Nano Research

Open Access

Research Article

Polarization-encodable photonic memory cells using next-generation 2D phase-change materials

Amin Shafiee[1,§], Linhong Chen[2,§], Mahdi Nikdast[1] ✉, and Jie Yao[2] ✉

[1] Department of Electrical and Computer Engineering, Colorado State University, Fort Collins, CO 80523, USA
[2] Department of Materials Science and Engineering, University of California, Berkeley, CA 94720, USA
[§] Amin Shafiee and Linhong Chen contributed equally to this work.

Cite this article: *Nano Research*, **2025**, *18*, 94907198. https://doi.org/10.26599/NR.2025.94907198

ABSTRACT: Integration of phase-change materials (PCMs) created a unique opportunity to implement reconfigurable photonics devices that their performance can be tuned depending on the target application. Conventional PCMs such as Ge-Sb-Te (GST) and Ge-Sb-Se-Te (GSST) rely on melt-quench and high temperature annealing processes to change the organization of the molecules in the materials' crystal. Such a reorganization leads to different optical, electrical, and thermal properties which can be exploited to implement photonic memory cells that are able to store the data at different resistance or optical transmission levels. Despite the great promise of conventional PCMs for realizing reconfigurable photonic memories, their slow and extremely power-hungry thermal mechanisms make scaling the systems based on such devices challenging. In addition, such materials do not offer a stable multi-level response over a long period of time. To address these shortcomings, the research carried out in this study shows the proof of concept to implement next-generation photonic memory cells based on two-dimensional (2D) birefringence PCMs such as SnSe, which offer anisotropic optical properties that can be switched ferroelectrically. We demonstrate that by leveraging the ultrafast and low-power crystallographic direction change of the material, the optical polarization state of the input optical signal can be changed. This enables the implementation of next-generation high-speed polarization-encodable photonic memory cells for future photonic computing systems. Compared to the conventional PCMs, the proposed SnSe-based photonic memory cells offer an ultrafast switching and low-loss optical response relying on ferroelectric property of SnSe to encode the data on the polarization state of the input optical signal. Such a polarization encoding scheme also reduces memory read-out errors and alleviates the scalability limitations due to the optical insertion loss often seen in optical transmission encoding.

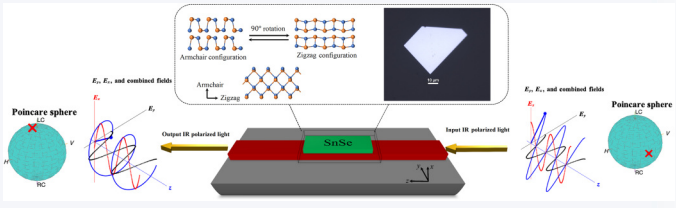

KEYWORDS: ferroelectric materials, phase-change materials, photonic memory, optical storage cells, polarization encodable photonic memories, optical polarization

1 Introduction

Photonic integrated circuits (PICs) have been deployed in a wide range of applications, from sensing and high-speed communication to energy-efficient optical computation in artificial intelligence (AI) accelerator systems [1–5]. More recently, phase change materials (PCMs) have been integrated with photonic devices to achieve reconfigurable photonic systems, such as photonic memory to selectively manipulate the light propagation to store data on the phase state of the PCMs [6–13]. The phase transition of PCMs leads to a drastic nonvolatile change in the material's optical and electrical properties, enabling the dynamic switching of PCM-based devices (i.e., multiple optical transmission or resistance levels). Despite the nonvolatile optical and electrical properties, conventional PCM-based photonic memory cells based on Ge-Sb-Te (GST) or Ge-Sb-Se-Te (GSST) rely on power-hungry and slow thermal mechanisms to initiate the phase transition via breaking down and changing the organization of the molecules in the PCM's crystal. This makes PCMs inefficient for memory applications [6, 7, 10, 14].

In contrast to the conventional PCMs, ferroelectric materials offer ultrafast switching speed and have been explored in low-power electronic device applications [12, 15]. Moreover, the switching process involves the change of polarization, i.e., the order parameter of ferroelectric materials, thus it has also been considered

Received: July 22, 2024; **Revised:** November 29, 2024
Accepted: December 13, 2024

✉Address correspondence to Mahdi Nikdast, Mahdi.Nikdast@colostate.edu; Jie Yao, yaojie@berkeley.edu

as a phase transition, making ferroelectric materials a novel type of PCM. However, most ferroelectric materials have two symmetric ground states with identical optical responses, hampering their photonic switching/memory applications. Group IV monochalcogenides (MXs, M = Ge or Sn; X = Sn or S) materials are polar compounds that form a puckered layer structure similar to that of the black phosphorus. The remarkable characteristic of MX materials lies in their unconventional ferroelectric response with 4 ground states that allow ultrafast transitions between distinct crystalline structures with strong optical anisotropy. As a result, such transition enables in-plane rotation of optical axes, leading to distinctive optical properties such as the polarization state related to the input light, when integrated with photonic devices [15–19]. Prior work showed that the fundamental limit on ferroelectric switching speed is set by the phonon-dispersion relation, and specifically the group velocity for acoustic phonons in the system (i.e., speed of sound), which determines on how fast the MX's lattice can respond [20]. The switching of the ferroelectric states of MX materials can be done by application of a strong electric field to the materials' crystal. In terms of the power requirements to change the ferroelectric state of ferroelectric materials, thermodynamic analysis showed that the power required for ferroelectric materials to change their ferroelectric state can be orders of magnitude more efficient than state of the art field-effect-transistors (FETs). Hence, the power required to change the ferroelectric state is significantly lower than the conventional PCMs such as GST and GSST [20–24].

Optical anisotropy arises when the optical properties of a material exhibit directional dependence [25–27]. In semiconductor materials, anisotropy can be attributed to factors such as crystal structure, molecular alignment, or electronic band structure. The directional dependence of the refractive index of an anisotropic material may lead to the change in the polarization state of the input light [25]. MX materials show giant in-plane anisotropy, making them bi-axial optical materials [26–29]. The crystalline structure of two nonvolatile ferroelectric states along the armchair and zigzag directions of SnSe is depicted in Fig. 1(a). More importantly, their orthorhombic structure with *Pnma* space group leads to the ferroelectric nature, allowing the in-plane crystalline orientation of the MX materials to be changed quickly through an ultrafast, nonthermal, and low-power electrical switching mechanism [22, 29]. As a result, the zigzag and armchair optical axes are swapped, in contrast to the conventional ferroelectric materials where optical responses do not change during the switching process. This mechanism can be exploited to implement optically controlled reconfigurable photonic devices. Assuming a linearly polarized light at the input, due to the birefringence property of SnSe, when changing the crystalline orientation of SnSe, the polarization state of the input light will change.

In this paper, we synthesized the thin film SnSe flakes on a silicon dioxide substrate using physical vapor deposition techniques and conducted careful optical characterization to capture the full optical parameter tensor in the near-infrared (IR) range which enables our design of polarization switchable waveguides.

Using our measurement set-up, we experimentally measured the optical transmission and reflection spectrum of the SnSe sample on a quartz substrate and then we exploited the measurement results incorporated with the relative transmission fringe depth (RTFD) method [30, 31] and our in-house solver based on Levenberg–Marquardt algorithm to numerically calculate the complex refractive index profile of the SnSe for a wide range of

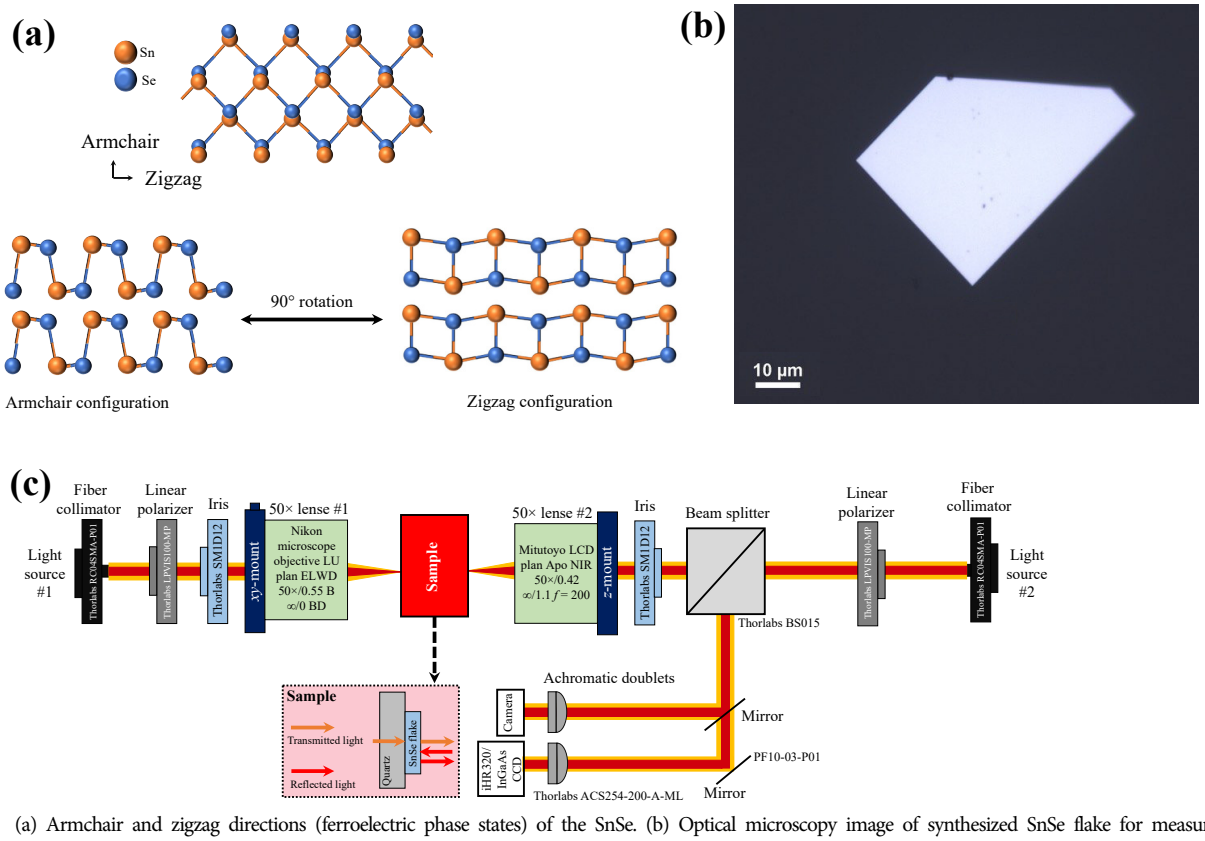

Figure 1 (a) Armchair and zigzag directions (ferroelectric phase states) of the SnSe. (b) Optical microscopy image of synthesized SnSe flake for measurements. (c) Measurement set-up to capture the intensity parameters in Eqs. (1) and (3) to calculate transmission and reflection spectrum of the fabricated SnSe flakes on the quartz substrate.

wavelengths. Eventually, we imported the calculated optical properties to a rigorous finite-difference time domain (FDTD) solver to accurately estimate the response of the proposed SnSe-based photonic memory cell using conventional silicon and silicon nitride waveguides. Using accurate three-dimensional (3D) FDTD simulations, we demonstrate the proof of concept of the fact that ferroelectric phase states of the SnSe as well as its birefringence properties make it a promising candidate to implement the next-generation photonic memory cells that are able to store the data by encoding it to the polarization state of the light instead of optical transmission by changing the ferroelectric phase state of the SnSe.

2 Experimental

2.1 Material preparation

The thin film SnSe sample was obtained by physical vapor deposition (PVD) method onto a clean SiO_2/Si substrate. 0.5 g of SnSe powers were placed at the center of a single-zone tube furnace (TF55035A-1 Thermo Scientific™) and a piece of silicon oxide substrate was placed downstream with a distance of ~ 9 cm from the power. During the growth process, SnSe powders were heated up to 500 °C within 70 min and were kept at this temperature for 4 h. SnSe was evaporated under this temperature and deposited onto silicon oxide substrate under the flow of carrier gas Ar/H_2 with a flow rate of 90 sccm. The growth pressure was kept at 40 Torr through the whole process. After the growth, thin SnSe single crystal flakes with relatively large sizes were identified and transferred onto a quartz substrate. The film thickness measured by atomic force microscopy (AFM; Oxford MFP-3D Origin+) was 383 nm [32, 33]. The microscopic image of a typical SnSe flake is reported in the Fig. 1(b).

2.2 Measuring optical reflection and transmission spectrum of SnSe

The optical transmission and reflection of SnSe sample onto quartz substrate were measured by our in-house set-up coupled to a Horiba iHR320 spectrometer and Horiba Symphony II InGaAs charge-coupled device (CCD) detector in the wavelength range from 1200 to 1800 nm using polarized light along the armchair (AC) and zigzag (ZZ) directions, respectively, generated by THORLABS SLS301 at normal incidence. The transmission $T(\lambda)$ and reflection $R(\lambda)$ were normalized according to the equations reported in Ref. [34] using the reflection spectrum of a clean gold mirror (Thorlabs PF10-03-M01) and transmission spectrum of a clean quartz substrate

$$T = \left(\frac{I_{ft}}{I_s}\right)(1 - R_q) \tag{1}$$

In Eq. (1), I_{ft} and I_s are the intensity of light transmitted through the film substrate system and the quartz reference, respectively, and R_q is the reflectance of quartz substrate and can be written as

$$R_q = \left(\frac{I_{qr}}{I_m}\right) R_m \tag{2}$$

The reflection spectrum of the SnSe can be written as

$$R = \left(\left(\frac{I_{fr}}{I_m}\right) R_m \left[(1 - R_q)^2\right]\right) - T^2 R_q \tag{3}$$

In Eq. (3), I_{fr} and I_m are the intensity of light reflected from the SnSe thin film and the gold mirror reference to the detector, respectively, and R_m is the reflectance of gold mirror depending on the property of reference mirror (Thorlabs PF10-03-P01). R_m has values above 97% for the wavelength range of 1–2 μm, hence, in our calculations, R_m assumed to have the value of 1. Note that I_{qr} is the intensity of the reflected light from the quartz substrate. The schematic diagram of the experimental set-up used to measure the optical transmission and reflection spectrum of the SnSe sample on top of the quartz substrate is depicted in Fig. 1(c). Moreover, the measured optical transmissions and reflections related to SnSe sample when the polarized light aligned with armchair and zigzag directions are reported in Figs. 2(a) and 2(b). Note that the intensity values to calculate the transmission and reflection spectrum are reported in Section S1 in the Electronic Supplementary Material (ESM).

2.3 Complex refractive index calculation of SnSe

With having the transmission and reflection spectrum of the thin film SnSe, the complex refractive index of the material could be calculated. In this paper the RTFD method was opted to use by solving Eqs. (4) and (5) reported in Refs. [30, 31, 33] to capture the complex refractive index of SnSe when the polarization of the input light was aligned with SnSe's armchair and zigzag direction

$$T(n,k) = \frac{T_1 T_2 \tau}{1 - 2\sqrt{R_1 R_2}\tau\cos\varphi + R_1 R_2 \tau^2} \tag{4}$$

$$R(n,k) = \frac{R_1 - 2\sqrt{R_1 R_2}\tau\cos\varphi + R_2\tau^2}{1 - 2\sqrt{R_1 R_2}\tau\cos\varphi + R_1 R_2 \tau^2} \tag{5}$$

where

$$R_1 = \frac{(n-1)^2 + k^2}{(n+1)^2 + k^2} = 1 - T_1$$

$$R_2 = \frac{(n-n_s)^2 + k^2}{(n+n_s)^2 + k^2} = 1 - T_2$$

$$\tau = \exp\left(-4\pi k\frac{d}{\lambda}\right), \quad \varphi = 4\pi n\frac{d}{\lambda}$$

where n_s and n are the refractive indices of substrate and film, respectively, k is the extinction coefficient of film, d is the film thickness, and λ is the operating wavelength. n_s can be calculated according to Eq. (6)

$$n_s = \frac{1 + \sqrt{R_q}}{1 - \sqrt{R_q}} \tag{6}$$

To solve the above equation system, we rearranged the above equations into the following forms according to Eqs. (7) and (8)

$$(\Delta R)^2 = (R(n,k) - R_{ex})^2 \tag{7}$$

$$(\Delta T)^2 = (T(n,k) - T_{ex})^2 \tag{8}$$

In Eqs. (7) and (8), R_{ex} and T_{ex} are the experimentally measured reflection and transmission spectrum of SnSe, respectively. By minimizing $(\Delta R)^2$ and $(\Delta T)^2$ using Levenberg–Marquardt algorithm [35], n and k can be calculated. In our calculation a set of (n, k) is accepted as a solution only if $(\Delta R)^2 + (\Delta T)^2 < 1 \times 10^{-30}$.

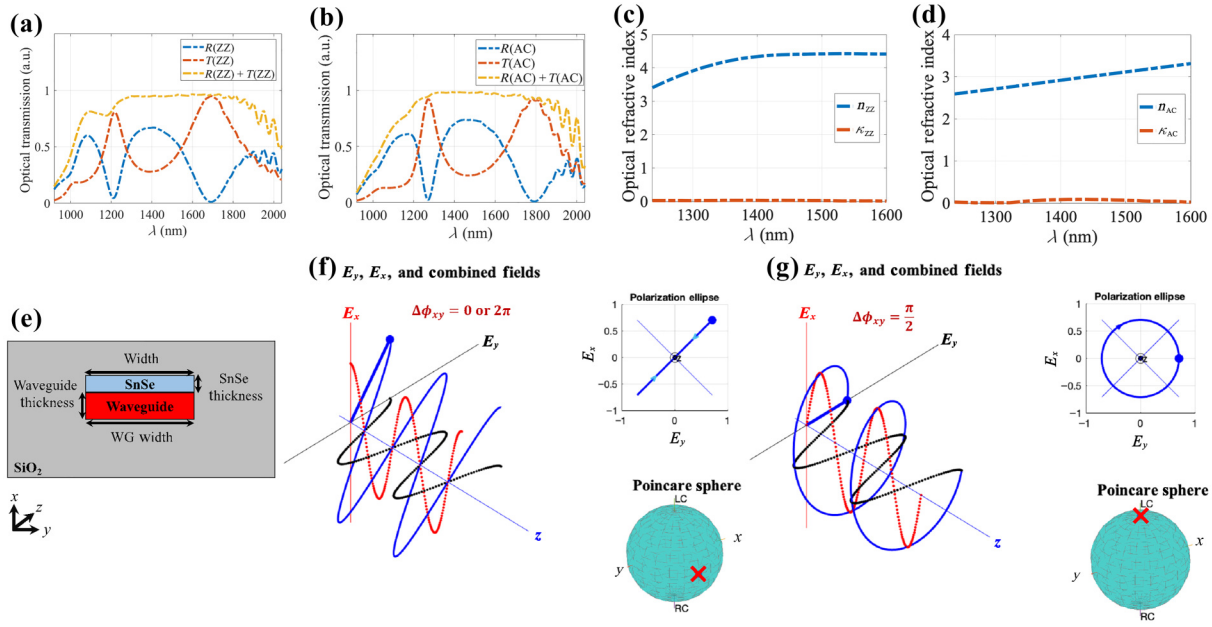

Figure 2 (a) Experimentally measured optical transmission and reflection results for the fabricated SnSe on the quartz substrate when the polarization of the light is aligned with SnSe's zigzag direction. (b) Experimentally measured optical transmission and reflection results for the fabricated SnSe on the quartz substrate when the polarization of the light is aligned with SnSe's armchair direction. (c) Calculated complex refractive index profile when the polarization of the light is aligned with zigzag direction. (d) Calculated complex refractive index profile when the polarization of the light is aligned with armchair direction. (e) Proposed SnSe-based photonic memory cell to encode the data on the phase-change stemmed polarization change of the light. (f) Schematic of a propagating optical planewave geometry when the polarization is linear (phase shift between the electric field components is either zero or 6.28 rad). (g) Schematic of a propagating optical planewave geometry when the polarization is circular (phase shift between the electric field components is $\frac{\pi}{2}$ rad).

3 Results and discussion

3.1 Optical properties of SnSe

In this section, we show the capability of SnSe to implement next-generation photonic memory cells using the light polarization to store the data instead of optical transmission which is the working principle of the conventional PCM-based photonic memory cells. SnSe is group IV monochalcogenide compounds with birefringence property, meaning that the optical refractive of the material is different for x, y, and z axes directions. The complex optical refractive index tensor of SnSe can be written as

$$\begin{pmatrix} n_{xx}+\mathrm{i}k_{xx} & 0 & 0 \\ 0 & n_{yy}+\mathrm{i}k_{yy} & 0 \\ 0 & 0 & n_{zz}+\mathrm{i}k_{zz} \end{pmatrix} \quad (9)$$

The transmission and reflection of the thin film SnSe are depicted in Figs. 2(a) and 2(b). Observe that for the C-band operating wavelength, the summation of reflection and transmission in both zigzag and armchair direction is unity, meaning that the material's absorption is significantly low.

Having the measured optical transmission and reflection spectrum, we numerically solved Eqs. (4) and (5) using an in-house solver based on the Levenberg–Marquardt algorithm to capture the complex refractive index of SnSe. The calculated results are shown in Figs. 2(c) and 2(d). Observe that when the alignment of the polarization of the input light changes from SnSe's armchair direction to zigzag direction, the real part of the optical refractive index changes for about 37%. This means that assuming polarized electromagnetic planewave interacting with the material, different electric field components of wave will develop different phase velocities. Assuming the armchair direction aligned with the z-direction and zigzag direction aligned with the y-direction, the optical refractive index tensor of SnSe at operating wavelength of 1550 nm can be written as

$$\begin{pmatrix} 4.15 & 0 & 0 \\ 0 & 4.42+0.016\mathrm{i} & 0 \\ 0 & 0 & 3.21+0.048\mathrm{i} \end{pmatrix} \quad (10)$$

Note that in this study, the refractive index of the bulk SnSe at operating wavelength of 1550 nm reported in Ref. [36] is used for the vertical component of the refractive index tensor along the x-axis. Moreover, there are other methods such as the one reported in Ref. [37] to capture the complex refractive index of materials. The results for complex refractive index of SnSe using the method in Ref. [37] are shown in detail in Section S2 in the ESM. Next, the characterized optical properties of SnSe derived in this section then will be imported in FDTD simulations in the next section to show how the ferroelectric phase change of SnSe can change the optical polarization properties of the input polarized light. In addition, the same set of calculation has been performed for a 31 nm thin SnSe sample in Section S3 in the ESM to verify the fact that optical properties are independent of the thickness of the sample.

3.2 Polarization-encodable SnSe-based photonic memory cells

The polarization of transverse electromagnetic planewaves describes the geometrical orientation of the oscillations related to its electrical and magnetic fields components. To better understand this, assuming a transverse optical planewave signal propagating in the free space with E_x and E_y electric field components excited, if the phase shift between the two excited components is zero, then the

optical signal will maintain a linear polarization with polarization angle of zero, as depicted in Fig. 2(f). This means that the optical planewave propagates with 45° of deviation with respect to x and y axes in the free space along the z-axis. Similarly, if we induce a 90° phase shift between the two excited electric field components, then the polarization of the input optical signal will be circularly polarized as it propagates with a circular geometry along the propagation direction (z-axis) in the free space, as is depicted in Fig. 2(g). Note that as the polarization angle of the planewave changes, its position on the Poincare sphere also changes due to the change of the Stokes parameters related to the propagating polarized light.

The tunable anisotropic optical refractive index of the SnSe can be used to selectively change the optical polarization of the input optical signal. This phenomenon can be used to implement next-generation reconfigurable photonic memories by integrating SnSe with conventional photonic devices. When a polarized optical signal interacts with a material with anisotropic optical properties, different components of the electric field develop different phases as a function of propagation length. Assuming a linearly polarized light at the input of the waveguide/SnSe cell depicted in Fig. 2(e), changing the lattice direction of the SnSe leads to achieving changes in polarization angle for a fixed geometry as different components of the electric field develop different phase shift along the propagation direction [38–40]. The experimentally characterized anisotropic refractive index profile of the SnSe in its distinct phase states can be imported into the FDTD solver provided by Ansys Lumerical to carry out the precise 3D FDTD electromagnetic simulation with a uniform 8-nm mesh size in all directions with a perfectly matched layer (PML) boundary condition [41]. For the proposed novel SnSe-based photonic memory cell, two different structures where the material for the waveguide is chosen to be silicon and silicon nitride are considered in this paper. Note that in the simulation presented in this work, the propagation direction is always considered to be the z-axis, the x-axis is along the thickness of the waveguide and SnSe and the y-axis is along the width of the waveguide and SnSe (see Fig. 2(e)). We start the performance analysis of SnSe-based photonic memory cells by simulating the optical loss of a SnSe-based photonic memory cells for: (a) When the armchair direction is aligned with the propagation direction and (b) when the zigzag direction is switched to the propagation direction. The results related to the optical loss for the two waveguide case studies are depicted in Fig. 3. Observe that for both silicon and silicon nitride waveguides, as the thickness of the SnSe increases, the optical loss per unit length also increases and the contribution of the SnSe width to the memory cell's optical loss is not as significant as the SnSe's thickness. Note that in our simulation study presented in this paper, the width of the waveguide is always equal to the width of SnSe. Moreover, observe that for the same design, the overall optical loss for silicon nitride waveguides (see Figs. 3(d) and 3(e)) is slightly higher than that for the silicon waveguides (see Figs. 3(a) and 3(b)). The reason for this is that at 1550 nm operating wavelength, the refractive index of silicon nitride is measured to be about 2 and for silicon is 3.48. Such a high refractive index value related to silicon compared to silicon nitride leads to higher mode confinement in the SnSe rather than the silicon nitride waveguide compared to the case where silicon waveguide is used. Note that in all of the simulations presented in this study, the thicknesses of silicon and silicon nitride waveguides are considered to be fixed at 310 and 600 nm, respectively, according to the CEA-leti foundry process-design-kit (PDK).

To calculate the polarization angle as a function of the length, the complex electric field components (E_x and E_y) of the input linearly polarized light are captured along the propagation length of the cell.

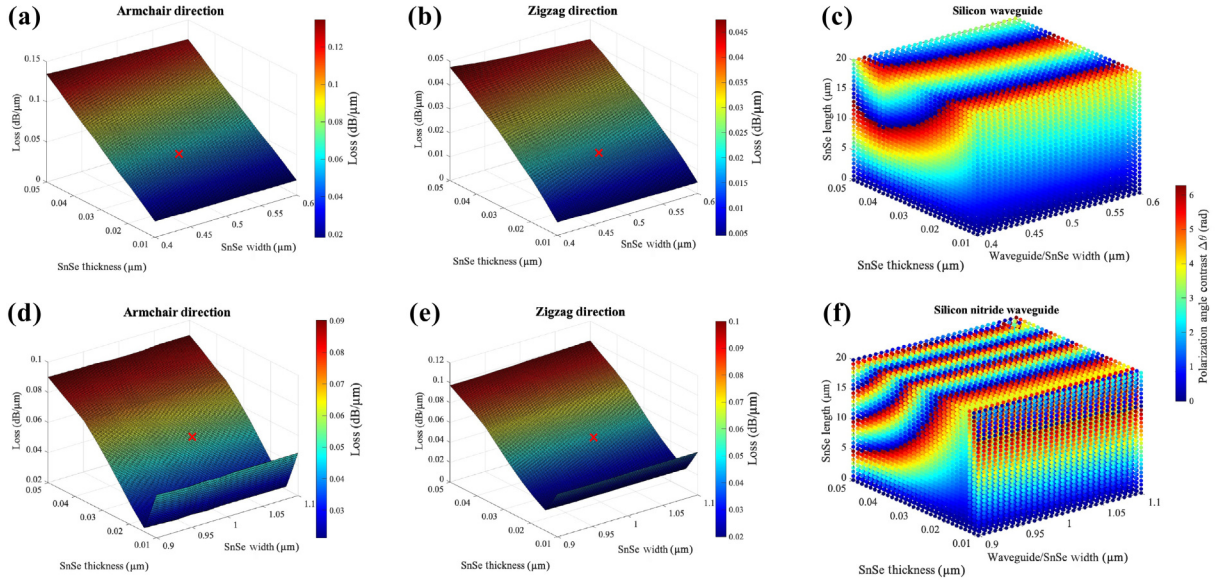

Figure 3 Design-space exploration of SnSe-based photonic memory cells using 3D FDTD simulations. (a) Optical insertion loss for silicon waveguide loaded with SnSe, and the propagation direction is aligned with SnSe's armchair direction. (b) Optical insertion loss for silicon waveguide loaded with SnSe and the propagation direction is aligned with SnSe's zigzag direction, (c) Design-space exploration of polarization angle contrast between zigzag and armchair directions when silicon waveguide is used. (d) Optical insertion loss for silicon nitride waveguide loaded with SnSe and the propagation direction is aligned with SnSe's armchair direction. (e) Optical insertion loss for silicon nitride waveguide loaded with SnSe and the propagation direction is aligned with SnSe's zigzag direction. (f) Design-space exploration of polarization angle contrast between zigzag and armchair directions when silicon nitride waveguide is used. The Red crosses on the figures denote the chosen design for SnSe-based photonic memory cell related to each case study. Note that the operating wavelength for all of the results is 1550 nm and the thicknesses of the waveguide for silicon and silicon nitride waveguides are considered to be fixed at 310 and 600 nm, respectively, according to the CEA-leti foundry PDK.

The maximum propagation length of the cell in our simulations is set to be 20 μm. Having the complex electric field profile along the length of the cell (z-axis), the polarization angle as a function of cell's length can be calculated according to Eq. (11)

$$\theta(L) = \mathrm{Tan}^{-1}\left(\frac{\mathrm{imag}(E_x(L))}{\mathrm{real}(E_x(L))}\right) - \mathrm{Tan}^{-1}\left(\frac{\mathrm{imag}(E_y(L))}{\mathrm{real}(E_y(L))}\right) \quad (11)$$

In Eq. (11), the first term denotes for the phase shift of the E_x and the latter term denotes the phase shift of E_y as a function of length. The achieved polarization angle contrast between the armchair and zigzag phase states of SnSe for silicon and silicon nitride waveguide as a function of SnSe's width, thickness, and length is depicted in Figs. 3(c) and 3(f). Observe that the rate of change in the polarization angle contrast for silicon nitride waveguide is faster than silicon one due to weaker mode confinement in the silicon nitride waveguides compared to silicon waveguides. Additionally, note that the effect of SnSe thickness is more significant than its width to induce the polarization angle contrast (see Figs. 3(c) and 3(f)). Considering the example maximum limit of 0.05 dB/μm for optical loss per unit length for the SnSe-based photonic memory cells [5], an example design with the SnSe thickness of 27 nm and widths of 500 and 1000 nm is considered for the cell based on silicon and silicon nitride waveguides, respectively. Such designs offer a relatively high polarization angle contrast while satisfying the given loss requirements (see Fig. 3(c)). Note that the chosen upper bound for optical insertion loss is significantly lower than the conventional optical transmission-encodable GST-based photonic memory cells which offer minimum 0.21 dB/μm optical insertion loss [6].

The polarization angle (θ) of the input polarized optical signal as a function of the propagation length along the z-axis for the chosen design related to SnSe-based photonic memory cell using silicon waveguides for the two ferroelectric phase states of zigzag and armchair is depicted in Fig. 4(a). Moreover, the corresponding Stokes parameters of S_2 and S_3 ($S_0 = E_x^2 + E_y^2 = 1$, $S_1 = E_x^2 - E_y^2 = 0$, $S_2 = 2E_xE_y\cos(\Delta\theta)$, and $S_3 = 2E_xE_y\sin(\Delta\theta)$, where $\Delta\theta$ is the polarization angle contrast between SnSe's armchair and zigzag directions) as a function of length are depicted in Figs. 4(b) and 4(c), respectively. Recall that the location of a polarized electromagnetic wave can be determined by its Stokes parameters. Furthermore, in this paper we opted to maximize the contrast in the S_2 parameter related to the polarized light. Observe that when the SnSe's length is 5.6 μm, the maximum contrast of $\Delta S_2 = 1.86$ with $\Delta\theta = 2.4$ rad between the two ferroelectric states can be achieved. This means that changing the phase state of the SnSe from armchair to zigzag direction or any intermediate state leads to the polarization state change of the light on the Poincare sphere within the range of $S_2 \in [-1, 0.86]$ at the output of the cell. This design leads to minimum loss of 0.28 dB when SnSe is in the armchair direction and 0.084 dB when the SnSe is in the zigzag direction.

The same analysis is carried out when the waveguide material is silicon nitride, and the results are reported in Figs. 4(d)–4(f). Note that for silicon nitride waveguide, due to its lower refractive index value, higher widths should be picked to ensure lossless propagation of input polarized light in the absence of SnSe layer. Observe that considering the mentioned loss requirement and the chosen design related to silicon nitride waveguides, when the length of SnSe on top of silicon nitride waveguide is 5 μm, the maximum $\Delta S_2 = 1.64$ with $\Delta\theta = 2.2$ rad can be achieved (see Figs. 3(f) and 4(d)–4(f)). This design leads to a minimum 0.19 dB and maximum 0.238 dB of

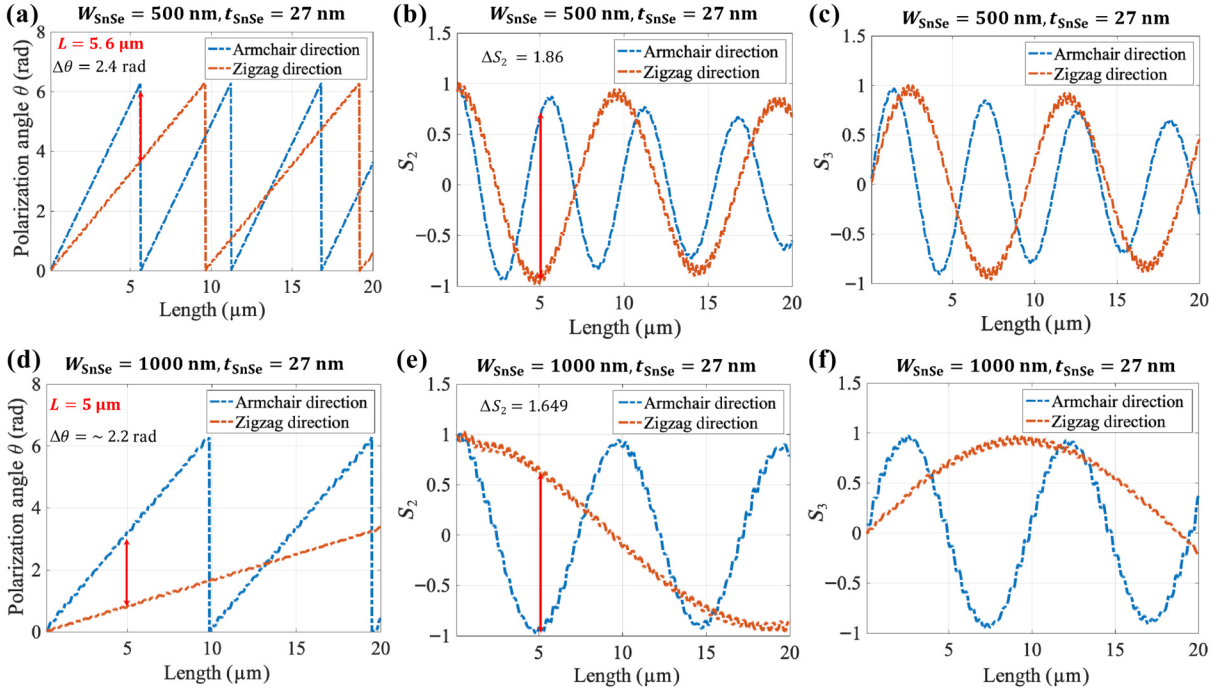

Figure 4 (a) Simulated polarization angle as a function of propagation length for the SnSe-based photonic memory cell using silicon waveguides when the width and thickness of the waveguide and the SnSe is 500 and 27 nm, respectively. (b) S_2 parameter of the SnSe-based photonic memory cell using silicon waveguide as a function of the length. (c) S_3 parameter of the SnSe-based photonic memory cell using silicon waveguides as a function of the length. (d) Simulated polarization angle as a function of propagation length for the SnSe-based photonic memory cell using silicon nitride waveguides when the width and thickness of the waveguide and the SnSe is 1 μm and 27 nm, respectively. (e) S_2 parameter of the SnSe-based photonic memory cell using silicon nitride waveguides as a function of the length. (f) S_3 parameter of the SnSe-based photonic memory cell using silicon nitride waveguides as a function of the length.

optical insertion loss, depending on the ferroelectric phase state of SnSe on top of the silicon nitride waveguide. Note that the achieved optical insertion loss values for SnSe-based photonic memory cells when silicon and silicon nitride waveguide is used are significantly lower than the conventional GST-based photonic memory cells with minimum 1 dB loss reported by Refs. [6, 9].

The polarization ellipse, the location of the polarized light on the Poincare sphere, and the geometry of the propagating electromagnetic wave for the designs picked in Fig. 4 when the SnSe is in the armchair and zigzag direction are depicted in Figs. 5(a)–5(d). Observe that when integrating with silicon and silicon nitride waveguides, and when SnSe has the armchair state, the polarization ellipse is close to the linear polarization while as the phase state of the SnSe changes to zigzag state, the light takes the elliptic polarization with higher ellipticity angles, which matches with the results presented in Fig. 4.

4 Conclusions

One of the fundamental bottlenecks in the conventional PCM-based photonic memory cells is that they rely on the power-hungry and time-consuming amorphous-crystalline phase transitions of the PCMs to encode the data on the optical transmission levels. In this study, for the first time, we showed the great potential of addressing the fundamental limitations related to conventional PCM-based photonic memories using a new class of PCMs called MX materials, namely SnSe. We first synthesized the SnSe flakes to experimentally characterize their optical properties for a wide range of operating wavelengths. Then, using rigorous 3D FDTD simulations, we showed the great promise of integration of SnSe with conventional photonic components such as photonic waveguides to implement polarization-encodable photonic memory cells. Compared to conventional optical transmission-encodable PCM-based photonic memories, SnSe-based photonic memories take advantage of optical polarization change to store the data on the material state. Moreover, the simulation results showed the significantly lower loss of the material compared to the conventional PCM-based photonic memory cells. In addition, we demonstrated that unlike the conventional PCM-based photonic memory cells, the proposed SnSe-based photonic memory cell's read-out is less sensitive to optical insertion loss as the data can be encoded in optical polarization levels rather than the optical transmission levels which can be affected by optical insertion loss. The study presented in this paper paves the way to realize next-generation scalable, ultrafast, energy-efficient, and high-performance photonic computing systems.

Electronic Supplementary Material: Supplementary material (intensity spectrum of transmitted light through and reflected light from SnSe and quartz substrate sample; second method to calculate the complex refractive index profile of SnSe; optical properties of 31-nm SnSe thin film; and SnSe's material yield) is available in the online version of this article at https://doi.org/10.26599/NR.2025.94907198.

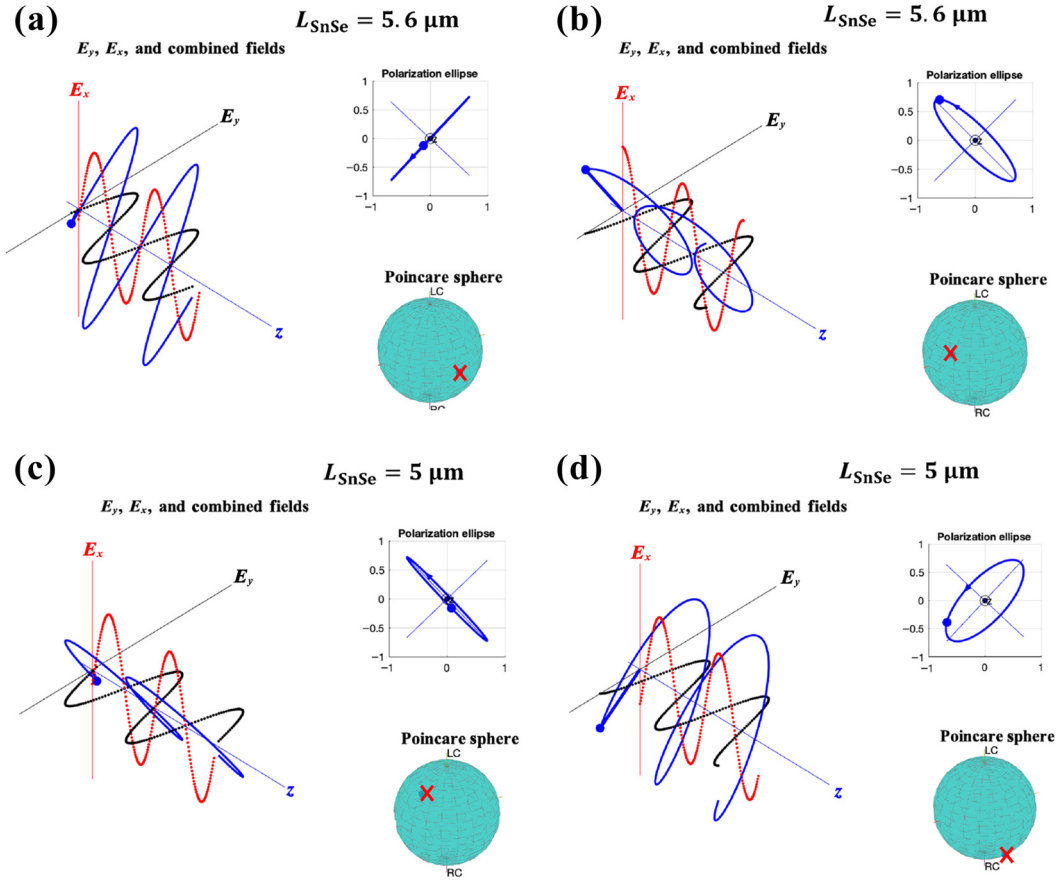

Figure 5 The geometrical shape of the polarized electromagnetic wave, the polarization ellipse, and its location on the Poincare sphere for the designs mentioned in Fig. 4 when (a) silicon waveguide is used with SnSe in armchair direction, (b) silicon waveguide is used with SnSe in zigzag direction, (c) silicon nitride waveguide is used with SnSe in armchair direction, and (d) silicon nitride is used with SnSe in the zigzag direction.

Data availability

All data needed to support the conclusions in the paper are presented in the manuscript and the Electronic Supplementary Material. Additional data related to this paper may be requested from the corresponding author upon request.

Acknowledgements

This work was supported by the National Science Foundation (NSF) (Nos. CCF-2006788 and CNS-2046226). L. H. C. and J. Y. thank the support of Heising-Simons Faculty Fellowship.

Declaration of competing interest

All the contributing authors report no conflict of interests in this work.

Author contribution statement

A. S.: Data curation, writing manuscript, doing the FDTD simulations. L. H. C.: Data curation, experimental design, data collection, data processing. M. N.: Project administration, funding acquisition. J. Y.: Project administration, funding acquisition. All the authors have approved the final manuscript.

Use of AI statement

None.

References

[1] Shafiee, A.; Pasricha, S.; Nikdast, M. A survey on optical phase-change memory: The promise and challenges. *IEEE Access* **2023**, *11*, 11781–11803.

[2] Shastri, B. J.; Huang, C. R.; Tait, A. N.; de Lima, T. F.; Prucnal, P. R. Silicon photonic neural network applications and prospects. In *Proceedings of AI and Optical Data Sciences III*, San Francisco, USA, 2022, pp 135–144.

[3] Ghanaatian, Z.; Shafiee, A.; Nikdast, M. Variation-aware layout and design optimization of silicon photonic Mach–Zehnder interferometers. In *Proceedings of 2023 IEEE Photonics Conference* (*IPC*), Orlando, USA, 2023, pp 1–2.

[4] Cheng, Z. G.; Ríos, C.; Youngblood, N.; Wright, C. D.; Pernice, W. H. P.; Bhaskaran, H. Device-level photonic memories and logic applications using phase-change materials. *Adv. Mater.* **2018**, *30*, 1802435.

[5] Sunny, F.; Shafiee, A.; Charbonnier, B.; Nikdast, M.; Pasricha, S. March. COMET: A cross-layer optimized optical phase-change main memory architecture. In *Proceedings of 2024 Design, Automation & Test in Europe Conference & Exhibition* (*DATE*), Valencia, Spain, 2024, pp 1–6.

[6] Xia, J.; Wang, T. C.; Wang, Z. X.; Gong, J. J.; Dong, Y. X.; Yang, R.; Miao, X. S. Seven bit nonvolatile electrically programmable photonics based on phase-change materials for image recognition. *ACS Photonics* **2024**, *11*, 723–730.

[7] Li, X.; Youngblood, N.; Ríos, C.; Cheng, Z. G.; Wright, C. D.; Pernice, W. H.; Bhaskaran, H. Fast and reliable storage using a 5 bit, nonvolatile photonic memory cell. *Optica* **2019**, *6*, 1–6.

[8] Pernice, W. H. P.; Bhaskaran, H. Photonic non-volatile memories using phase change materials. *Appl. Phys. Lett.* **2012**, *101*, 171101.

[9] Ríos, C.; Stegmaier, M.; Hosseini, P.; Wang, D.; Scherer, T.; Wright, C. D.; Bhaskaran, H.; Pernice, W. H. P. Integrated all-photonic non-volatile multi-level memory. *Nat. Photon.* **2015**, *9*, 725–732.

[10] Fang, Z. R.; Chen, R.; Zheng, J. J.; Khan, A. I.; Neilson, K. M.; Geiger, S. J.; Callahan, D. M.; Moebius, M. G.; Saxena, A.; Chen, M. E. et al. Ultra-low-energy programmable non-volatile silicon photonics based on phase-change materials with graphene heaters. *Nat. Nanotechnol.* **2022**, *17*, 842–848.

[11] Shafiee, A.; Charbonnier, B.; Pasricha, S.; Nikdast, M. Design space exploration for PCM-based photonic memory. In *Proceedings of the Great Lakes Symposium on VLSI 2023*, Knoxville, USA, 2023, pp 533–538.

[12] Aryana, K.; Kim, H. J.; Popescu, C. C.; Vitale, S.; Bae, H. B.; Lee, T.; Gu, T.; Hu, J. J. Toward accurate thermal modeling of phase change material-based photonic devices. *Small* **2023**, *19*, 2304145.

[13] Yu, J. B.; Luo, M. T.; Lv, Z. Y.; Huang, S. M.; Hsu, H. H.; Kuo, C. C.; Han, S. T.; Zhou, Y. Recent advances in optical and optoelectronic data storage based on luminescent nanomaterials. *Nanoscale* **2020**, *12*, 23391–23423.

[14] Shafiee, A.; Charbonnier, B.; Yao, J.; Pasricha, S.; Nikdast, M. Programmable phase change materials and silicon photonics co-integration for photonic memory applications: A systematic study. *J. Opt. Microsyst.* **2024**, *4*, 031208.

[15] Li, X.; Liu, H. Y.; Ke, C. M.; Tang, W. Q.; Liu, M. Y.; Huang, F. H.; Wu, Y. P.; Wu, Z. M.; Kang, J. Y. Review of anisotropic 2D materials: Controlled growth, optical anisotropy modulation, and photonic applications. *Laser Photonics Rev.* **2021**, *15*, 2100322.

[16] Chen, Z. G.; Shi, X. L.; Zhao, L. D.; Zou, J. High-performance SnSe thermoelectric materials: Progress and future challenge. *Prog. Mater. Sci.* **2018**, *97*, 283–346.

[17] Lin, Y. C.; Torsi, R.; Younas, R.; Hinkle, C. L.; Rigosi, A. F.; Hill, H. M.; Zhang, K. Y.; Huang, S. X.; Shuck, C. E.; Chen, C. et al. Recent advances in 2D material theory, synthesis, properties, and applications. *ACS Nano* **2023**, *17*, 9694–9747.

[18] Li, F.; Wang, H. D.; Huang, R. J.; Chen, W. W.; Zhang, H. Recent advances in SnSe nanostructures beyond thermoelectricity. *Adv. Funct. Mater.* **2022**, *32*, 2200516.

[19] Shi, W. R.; Gao, M. X.; Wei, J. P.; Gao, J. F.; Fan, C. W.; Ashalley, E.; Li, H. D.; Wang, Z. M. Tin selenide (SnSe): Growth, properties, and applications. *Adv. Sci.* **2018**, *5*, 1700602.

[20] Shi, Q. W.; Parsonnet, E.; Cheng, X. X.; Fedorova, N.; Peng, R. C.; Fernandez, A.; Qualls, A.; Huang, X. X.; Chang, X.; Zhang, H. R. et al. The role of lattice dynamics in ferroelectric switching. *Nat. Commun.* **2022**, *13*, 1110.

[21] Ramesh, R.; Manipatruni, S. Electric field control of magnetism. *Proc. Roy. Soc. A* **2021**, *477*, 20200942.

[22] Jo, S. S.; Wu, C. M.; Zhu, L. H.; Yang, L.; Li, M.; Jaramillo, R. Photonic platforms using in-plane optical anisotropy of tin(II) selenide and black phosphorus. *Adv. Photonics Res.* **2021**, *2*, 2100176.

[23] Wang, H.; Qian, X. F. Two-dimensional multiferroics in monolayer group IV monochalcogenides. *2D Mater.* **2017**, *4*, 015042.

[24] Hanakata, P. Z.; Carvalho, A.; Campbell, D. K.; Park, H. S. Polarization and valley switching in monolayer group-IV monochalcogenides. *Phys. Rev. B* **2016**, *94*, 035304.

[25] Wang, J.; Jiang, C. Z.; Li, W. Q.; Xiao, X. H. Anisotropic low-dimensional materials for polarization-sensitive photodetectors: From materials to devices. *Adv. Opt. Mater.* **2022**, *10*, 2102436.

[26] Kumar, M.; Rani, S.; Singh, Y.; Gour, K. S.; Singh, V. N. Tin-selenide as a futuristic material: Properties and applications. *RSC Adv.* **2021**, *11*, 6477–6503.

[27] Xu, X. L.; Song, Q. J.; Wang, H. F.; Li, P.; Zhang, K.; Wang, Y. L.; Yuan, K.; Yang, Z. C.; Ye, Y.; Dai, L. In-plane anisotropies of

polarized Raman response and electrical conductivity in layered tin selenide. *ACS Appl. Mater. Interfaces* **2017**, *9*, 12601–12607.

[28] Titova, L. V.; Fregoso, B. M.; Grimm, R. L. Group-IV monochalcogenides GeS, GeSe, SnS, SnSe. In *Chalcogenide*. Liu, X. Y.; Lee, S.; Furdyna, J. K.; Luo, T. F.; Zhang, Y. H., Eds.; Elsevier: Amsterdam, 2020; pp 119–151.

[29] Yang, S. X.; Liu, Y.; Wu, M. H.; Zhao, L. D.; Lin, Z. Y.; Cheng, H. C.; Wang, Y. L.; Jiang, C. B.; Wei, S. H.; Huang, L. et al. Highly anisotropic optical and electrical properties in layered SnSe. *Nano Res.* **2018**, *11*, 554–564.

[30] Yinping, Z.; Chuang, Z.; Xinshi, G.; Xingang, L. A precise and simple method, the relative transmission fringe depth method, of determining the optical constants and thickness of thin semitransparent films. *J. Phys. D: Appl. Phys.,* **1992**, *25*, 1004–1009.

[31] Baban, C.; Rusu, G. G.; Nicolaescu, I. I.; Rusu, G. I. Optical properties of CdSe films deposited by the quasi-closed volume technique. *J. Phys.: Condens. Matter* **2000**, *12*, 7687–7697.

[32] Tomlin, S. G. Optical reflection and transmission formulae for thin films. *J. Phys. D: Appl. Phys.* **1968**, *1*, 1667–1671.

[33] Wu, Q.; Fang, Z. X.; Zhu, Y. L.; Song, H. Z.; Liu, Y.; Su, X.; Pan, D. F.; Gao, Y.; Wang, P.; Yan, S. C. et al. Controllable edge epitaxy of helical GeSe/GeS heterostructures. *Nano Lett.* **2022**, *22*, 5086–5093.

[34] El-Nahass, M. M.; El-Deeb, A. F.; Metwally, H. S.; El-Sayed, H. E. A.; Hassanien, A. M. Influence of X-ray irradiation on the optical properties of iron(III) chloride tetraphenylporphyrin thin films. *Solid State Sci.* **2010**, *12*, 552–557.

[35] Ranganathan, A. The levenberg-marquardt algorithm. *Tutoral on LM Algorithm* **2004**, *11*, 101–110.

[36] John, K. J.; Pradeep, B.; Mathai, E. Tin selenide (SnSe) thin films prepared by reactive evaporation. *J. Mater. Sci.* **1994**, *29*, 1581–1583.

[37] Murmann, H. Der spektrale Verlauf der anomalen optischen Konstanten dünnen Silbers. *Z. Phys.* **1936**, *101*, 643–648.

[38] Halevi, P. Plane electromagnetic waves in material media: Are they transverse waves. *Am. J. Phys.* **1980**, *48*, 861–867.

[39] Papas, C. H. *Theory of Electromagnetic Wave Propagation*; Courier Corporation: North Chelmsford, 2014.

[40] Kong, J. A. *Theory of Electromagnetic Waves*; Wiley: New York, 1975.

[41] Ansys. *Lumerical is Now Part of the Ansys Family* [Online]. https://www.lumerical.com (accessed Jul 15, 2024).